remote sensing

MDPI

Article

The Application of ALOS/PALSAR InSAR to Measure Subsurface Penetration Depths in Deserts

Siting Xiong [1,*], Jan-Peter Muller [1] and Gang Li [2]

[1] Imaging Group, Mullard Space Science Laboratory (MSSL), Department of Space & Climate Physics, University College London, Holmbury St Mary, Dorking, Surrey RH5 6NT, UK; j.muller@ucl.ac.uk

[2] Institute of Space and Earth Information Science, The Chinese University of Hong Kong, New Territories, Hong Kong, China; ligang@link.cuhk.edu.hk

* Correspondence: siting.xiong.14@ucl.ac.uk; Tel.: +44-1483-204-926; Fax: +44-1483-278-312

Academic Editor: Richard Gloaguen

Received: 14 April 2017; Accepted: 16 June 2017; Published: 21 June 2017

Abstract: Spaceborne Synthetic Aperture Radar (SAR) interferometry has been utilised to acquire high-resolution Digital Elevation Models (DEMs) with wide coverage, particularly for persistently cloud-covered regions where stereophotogrammetry is hard to apply. Since the discovery of sand buried drainage systems by the Shuttle Imaging Radar-A (SIR-A) L-band mission in 1982, radar images have been exploited to map subsurface features beneath a sandy cover of extremely low loss and low bulk humidity in some hyper-arid regions such as from the Japanese Earth Resources Satellite 1 (JERS-1) and Advanced Land Observing Satellite/Phased Array type L-band Synthetic Aperture Radar (ALOS/PALSAR). Therefore, we hypothesise that a Digital Elevation Model (DEM) derived by InSAR in hyper-arid regions is likely to represent a subsurface elevation model, especially for lower frequency radar systems, such as the L-band system (1.25 GHz). In this paper, we compare the surface appearance of radar images (L-band and C-band) with that of optical images to demonstrate their different abilities to show subsurface features. Moreover, we present an application of L-band InSAR to measure penetration depths in the eastern Sahara Desert. We demonstrate how the retrieved L-band InSAR DEM appears to be of a consistently 1–2 m lower elevation than the C-band Shuttle Radar Topography Mission (SRTM) DEM over sandy covered areas, which indicates the occurrence of penetration and confirms previous studies.

Keywords: subsurface mapping; hyper-arid regions; InSAR; radar backscatter; ALOS/PALSAR

1. Introduction

Hyper-arid regions remain one of the most desolate and inhospitable places on Earth. However, some of them host many subsurface natural resources, such as oil, gas, groundwater, etc. The exploitation of these subsurface resources needs substantial reconnaissance work, such as field surveys and in-situ measurements, which can be very time and labour consuming and hence costly. Nowadays, with the development of various spaceborne and airborne remote sensors at microwave frequencies, it may be feasible to study the subsurface part of hyper-arid regions. The successful acquisition of L-band SAR images by SEASAT in 1978 [1] led to several follow-up missions: SIR-A (1981), SIR-B (1984), and two SIR-C/X-SAR missions (1994). These missions revealed that at L-band wavelengths, radar has a limited penetration ability over the Eastern Sahara [2], although coverage with penetration was very limited.

Regarding the ability to identify subsurface features, SAR images are superior to optical images because their longer wavelength leads to subsurface penetration [1,2]. The penetration of waves occurs under the condition of a small scattering loss within the surface cover layer, which has grain sizes smaller than 10% of the incident wavelength and has a moisture content of less than 1% [3].

Thus, hyper-arid regions covered by fine-grained, homogeneous, and sufficiently dry materials are favourable areas where radar penetration is likely to occur. The skin depth was calculated as ~0.1–0.3 m for X-band (λ = 3 cm), ~0.2–0.5 m for C-band (λ = 5.7 cm), and ~1.5–2 m for L-band (λ = 23.5 cm) based on samples collected from the Selima Sand Sheet [4]. The penetration depth at L-band was suspected to be deeper than 2 m because the paleo-channels are visible in SIR-A's L-band (e.g., 1.25 GHz/24 cm, L-band) images, while they are buried at more than 2 m under the sand cover in several locations of the Selima Sand Sheet [2,5].

Following the SIR-A/B/C missions, studies of a C-band SRTM DEM in 2000 [6,7], Radarsat-2 images in 2006 [5,8], and the ALOS/ PALSAR imagery in 2009 [9–12] also showed the paleo-channels in the Eastern Sahara. During the last few decades, studies in hyper-arid regions have mainly taken advantage of: (1) radar backscatter data (image tones) [6–15]; (2) InSAR derived topographic data [16–18]; and (3) polarimetric SAR data [19,20]. Amongst these, InSAR derived topography is a direct measurement which allows an investigation of the differing penetration abilities at different radar wavelengths. It is important to study the differences between the InSAR DEMs derived at differing wavelengths and DEMs generated by techniques such as stereophotogrammetry and Light Detection and Raging (LiDAR) [21–27]. To take full advantage of these DEMs and to apply them in various applications, it is necessary to study the location in the subsurface that these DEMs refer to.

In this study, we will explore two aspects of L-band radar images. Firstly, we will compare the surface morphology of radar images, optical images, and DEMs to study their differing abilities to reveal subsurface features. Secondly, we will focus on comparing differing elevations detected by ALOS/PALSAR and SRTM C-band DEM by using differential SAR interferometry and comparing this with elevation data from Ice, Cloud, and land Elevation Satellite (ICESat) to evaluate the penetration depth which can be measured by L-band SAR imagery.

2. Study Site

Kufra is in southeastern Libya and is within the Eastern Sahara region. By using Radarsat-1 C-band (5.6 GHz/5.5 cm) images, Robinson et al. interpreted subsurface paleo-drainage, which passes through this region from south to east until Sarir Dalmah in Libya [5,28]. This paleo-drainage does not coincide with that recorded in the United States Geological Survey (USGS) HYDRO1k database in this area, which suggests that it may be of subsurface origin [5]. Following this, a more complete L-band radar coverage of the eastern Sahara by the Japanese JERS-1 satellite was used to create the first regional-scale radar mosaic covering Egypt, northern Sudan, eastern Libya, and northern Chad [29]. Subsequently, ALOS/PALSAR L-band data allowed, for the first time, an accurate mapping of a continuous 900 km-long paleo-drainage system, which is termed the Kufra River [10].

The sand cover layer in this area overlies the Nubian Sandstone Series, which are composed of sands, sandstones, clays, and shales [30,31]. The Nubian Sandstone Aquifer System (NSAS) is the largest known fossil water aquifer system on Earth. It is located underground in the Eastern Sahara Desert and spans just over 2,000,000 km^2, including north-western Sudan, north-eastern Chad, south-eastern Libya, and most of Egypt [32]. It contains an estimated 150,000 km^3 of groundwater [33]. The aquifer is mainly composed of hard ferruginous sandstone with shale and clay intercalation, having a thickness that ranges between 140–230 m [33].

Our study site is selected to be situated over one of the eastern tributaries of the Kufra River, which arises in northern Uweinat close to the Sudanese border and is named the Uweinat tributary [5]. The coverage (centre latitude and longitude are 23.265°N, 23.603°E) of the InSAR image pair is shown as a red rectangle in Figure 1a. Figure 1b shows the ALOS/PALSAR HH amplitude image, along with three close-up pictures from Google Earth to show three bright spots in the ALOS/PALSAR HH amplitude image. Figure 1(c1,c2) display two areas which appear to be plants covered by sand and Figure 1(c3) shows an area which seems to be outcrop rocks.

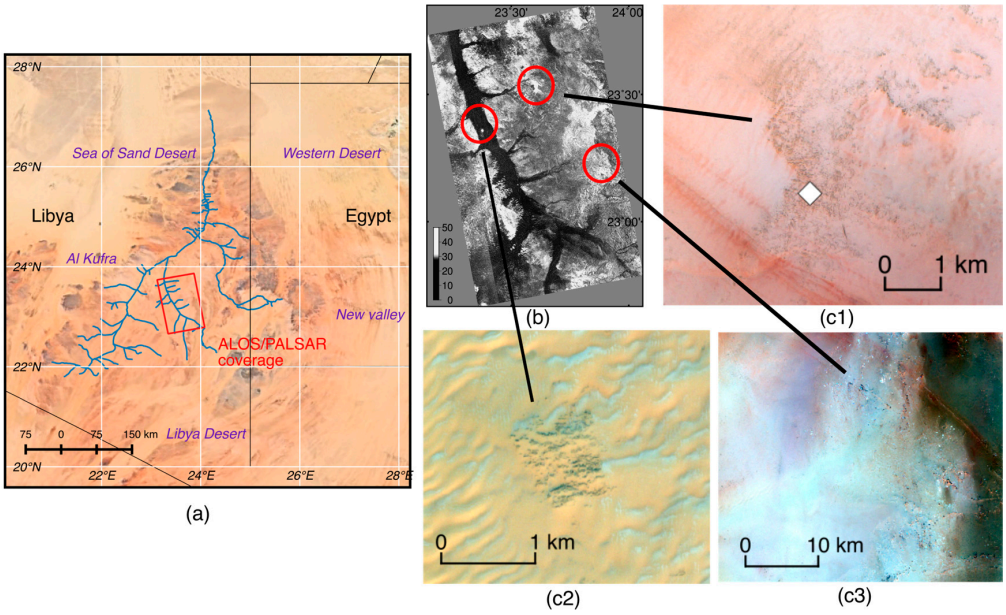

Figure 1. (**a**) Satellite image coverage of the study site. The background image is from Google Earth and is georeferenced in QGIS. The blue lines denote the paleo-drainage system which is visible within the ALOS/PALSAR image [12]. The red rectangle is the coverage of one ALOS/PALSAR frame, which shows the study site; (**b**) the ALOS/PALSAR HH amplitude image (70 × 110 km); (**c1**–**c3**) show three areas: (**c1**) appears to be the plants covered by sand (white diamond denotes the location of a reference point used in InSAR processing), (**c2**) showing a bright spot in the channel area (**b**), which also appears to be plants covered by sand and (**c3**) showing a bright area in the ALOS/PALSAR image, which may be outcrop rocks.

3. Data and Methods

3.1. Comparison of Image Surface Morphology

The occurrence of radar penetration in the Selima Sand Sheet in the Eastern Sahara, where there is a fine-grained sand cover, was first revealed by comparing radar images with visible images [2]. The buried subsurface features appear in radar images, while remain unobserved in corresponding visible images. The radar waves can penetrate the sandy cover layer and are less likely to be reflected or scattered at the surface, mainly attributed to its longer wavelength. The occurrence and brightness of subsurface features in radar images depends on many factors, including the wavelength, incidence angle, aspect angle, polarisation of the incident wave, surface roughness, grain size, moisture, etc. Dark tones in the radar images indicate low backscatters, which can be explained by two scenarios. One scenario suggests a smooth surface of the radar wavelength λ, which causes specular reflection of the incident radar waves. Alternatively, the incident radar wave penetrates into the sand layer and is absorbed or scattered in this sandy cover material. In this condition, the volume scattering V is usually high enough to cause a large volume scattering loss within the covering material. On the other hand, the bright tone in the radar image, indicates higher backscatter, which may be caused by outcropping rocks with a large radar cross section. The medium tone can be explained by a rough surface if no penetration occurs or by the scenario in which the radar wave transmits into the subsurface and is reflected by a shallow layer, while part of the wave energy is absorbed or scattered during the transition between the surface and subsurface layer.

In this study, we compare the surface morphology of an L-band ALOS/PALSAR image against an optical image from Landsat, an SAR image, and DEM from C-band SRTM. The SRTM [21] was an 11-day mission, which aimed to produce a near global DEM with a resolution of up to 1 arc-second

(≈30 m). Apart from the global DEM, the mission also provides a C-band combined image (sub-swath images of HH and VV are combined [34]).

3.2. SAR Interferometry

3.2.1. Interferometic Phase Formation

SAR interferometry is used to calculate the interference pattern caused by the difference in phases between the two images acquired by a space-borne SAR, which is usually processed from two repeat passes of the satellite at two different times. Figure 2 shows the geometry of SAR interferometry. The resulting difference of phases (wrapped in the range of $[-\pi, \pi]$) forms a new kind of image called an interferogram. Equation (1) shows the formation of the interferogram. M and S are the master and slave images, respectively, and I_m, I_s, φ_m, φ_s denote the intensities and phases of the master and slave images. The interferometric phase, $\Delta\varphi$, a pattern of fringes containing all of the information on the relative geometry, including contributions of the topography φ_{top}, the orbital trajectories φ_{orb}, atmospheric effects including φ_{tro} from the troposphere and φ_{ion} from the ionosphere, surface displacement φ_{dis}, and phase resulting from speckle noise φ_{noi}. These phase components can be expressed as Equation (2) [35].

$$Int = M * S = |I_m||I_s| \exp[j(\varphi_m - \varphi_s)], \tag{1}$$

$$\begin{aligned} \Delta\varphi = \varphi_m - \varphi_s &= \varphi_{top} + \varphi_{orb} + \varphi_{tro} + \varphi_{ion} + \varphi_{dis} + \varphi_{noi} \\ \varphi_{dif} &= \varphi_{orb} + \varphi_{tro} + \varphi_{ion} + \varphi_{dis} + \varphi_{noi} \end{aligned} \tag{2}$$

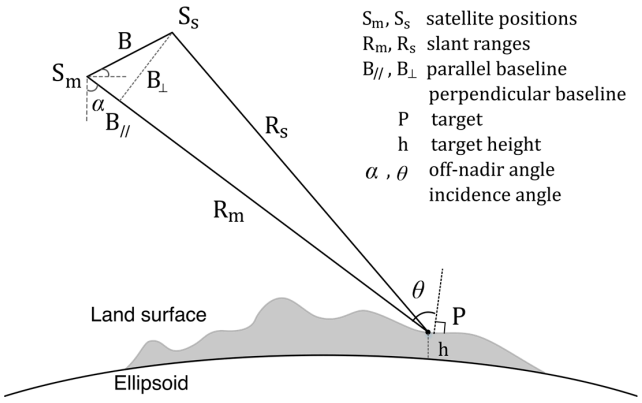

Figure 2. The geometry of SAR Interferometry. The subscripts of m and s denote the master and slave images of an InSAR image pair.

In conventional differential SAR interferometry, the remaining phase after removing the orbital and topographic phase, which is termed the differential phase, should include φ_{tro}, φ_{ion}, φ_{dis}, and φ_{noi}. However, if an L-band SAR image pair is utilised to form an interferogram and an external C-band SRTM DEM is employed to simulate the topographic phase, an additional phase component, φ_{ele_dif}, which results from the difference between L- and C-band, should be included. Therefore, the differential phase in Equation (2) changes into Equation (3). Equations (4) and (5) express the phases caused by topographic variation p and surface displacement d, where $B_\perp$, R, θ are the perpendicular baseline, slant range, and incident angle, respectively. A flowchart of the InSAR processing and analysis of phase components is shown in Figure 3.

$$\varphi_{dif} = \varphi_{orb} + \varphi_{ion} + \varphi_{tro} + \varphi_{dis} + \varphi_{ele\_dif} + \varphi_{noi} \tag{3}$$

$$\varphi_{ele\_dif} = -\frac{4\pi}{\lambda}\frac{B_{\perp}}{Rsin\theta}p \tag{4}$$

$$\varphi_{dis} = -\frac{4\pi}{\lambda}d \tag{5}$$

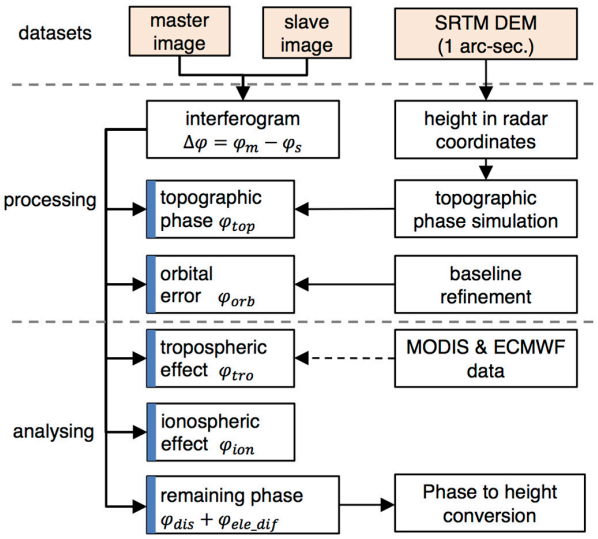

Figure 3. Flowchart of InSAR processing and analyses of phase components used in this study. The interferograms contains phase contributions from topography, orbital error, tropospheric and ionospheric delay, and the remaining phase. The remaining phase can be caused by surface displacement, topographic phase residual, which may result from the different penetration depths detected by L- and C-band SAR.

SAR data from ALOS/PALSAR is processed using InSAR in this study. ALOS/PALSAR [24] is a radar system launched by the Japan Aerospace Exploration Agency (JAXA) that can also be used to derive high resolution DEMs at 30 m. Four acquisitions of ALOS/PALSAR data are collected and their key features are listed in Table 1. The ALOS/PALSAR acquisitions are from ascending orbits of 13 August 2007, 13 February 2008, 30 September 2008, and 31 December 2008, respectively. Two of them are acquired in the Fine Beam Dual (FBD) polarisation of HH and HV, while two of them are obtained in the Fine Beam Single (FBS) polarisation of HH. HH polarisation is used to form interferograms. The incident angle is 34.3° for all acquisitions. In this study, we used the Repeat Orbit Interferometry PACkage, ROI_PAC [36], developed by the National Aeronautics and Space Administration (NASA)'s Jet Propulsion Laboratory (JPL), to generate interferograms.

Table 1. Information on the four ALOS/PALSAR acquisitions.

Acquisition Dates	Orbit Numbers	Path	Frame	Polarisation	Product Type
13 August 2007	8268	627	450	HH/HV	Level 1.0 raw data
13 February 2008	10952			HH	
30 September 2008	14307			HH/HV	
31 December 2008	15649			HH	

InSAR utilises the phase differences of the waves, so it requires signals from two different acquisitions to be coherent. Multi-look processing is a traditional method to reduce phase noise in SAR processing, while it reduces the resolution of interferograms. The phase noise can be estimated from the interferometric SAR pair using coherence. The coherence is the cross-correlation coefficient of the SAR image pair, which is estimated over a small window (a few pixels in range and azimuth). The

theoretical elevation dispersion (standard deviation) can be calculated from the perpendicular baseline and coherence as Equation (6) [37].

$$\sigma_h = -\frac{\lambda R sin\theta}{4\pi B_\perp} \cdot \sigma_\phi = -\frac{\lambda R sin\theta}{4\pi B_\perp} \cdot \frac{1}{\sqrt{2NL}} \cdot \frac{\sqrt{1-r^2}}{r}, \quad (6)$$

where λ is the wavelength, R is the range, θ is the incidence angle, $B_\perp$ is the perpendicular baseline, and NL, r are the number of looks and coherence, respectively. Figure 4a shows the relationship between coherence and elevation dispersion for different perpendicular baselines when NL = 8, while Figure 4b presents the relationship between coherence and elevation dispersion for different numbers of looks when the perpendicular baseline is set to 2000 m. We set NL = 8 to improve the coherence and maintain the spatial resolution (range direction is ~37 m and azimuth direction is ~56 m) in this study. We can see from Figure 5 that the coherence above 0.218 leads to an elevation dispersion within 5 m when the perpendicular baseline is 2000 m and NL = 8.

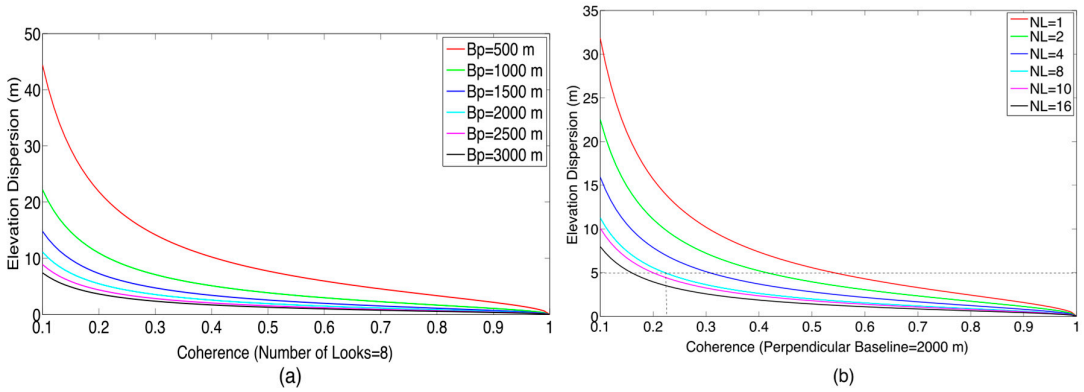

Figure 4. Relationship between coherence and elevation dispersion in (**a**) different perpendicular baselines and (**b**) different numbers of looks; Coherence needs to be above 0.218 to limit elevation dispersion below 5 m when NL = 8 and PB = 2000 m are applied (Parameters used in the calculation is from ALOS/PALSAR system: $\lambda = 0.236$ m, $R = 843,343$ m and $\theta = 34.3°$).

3.2.2. Removal of Topographic and Orbital Phase

Topography is one of the main contributions to the interferometric phase $\Delta\varphi$. Topographic phase, φ_{top}, yields fringes that hug the topography that looks like contour lines. Topographic phase can be simulated by using an available external DEM. The external DEM used to simulate topographic phase is SRTM C-band DEM (Version 3, resolution of 1-arc second ~30 m). Table 2 lists the characteristics of these two systems. The SRTM DEM heights are referenced to the Earth Gravitational 1996 (EGM96) geoid, while the World Geodetic System (WGS84) ellipsoid is used in InSAR processing. We converted the datum of SRTM C-band DEM from EGM96 to WGS84 by using an EGM96 15′ geoid height model [38].

The orbital phase φ_{orb}, which is another contribution to the $\Delta\varphi$, is caused by the orbital trajectories. It can be removed given the knowledge of the satellite trajectories. For some missions, this knowledge is not accurate to the scale of the wavelength, leading to errors in the baseline estimation and leaving regular fringes in the interferogram. These periodic fringes can be used in turn to refine the relative separation between the two trajectories, which is termed as baseline refinement. In ROI_PAC, the baseline refinement is realised by a quadratic model fitted between the total phase and surface elevation from an external topographic data source [37]. Baseline refinement is applied to the interferograms when periodic fringes are observed after removing topographic orbital phase. The remaining phase is unwrapped by using the phase unwrapping algorithm, the Statistical-cost, Network-flow Algorithm for Phase Unwrapping (SNAPHU) [39].

Table 2. Systematic parameters of ALOS/PALSAR FBD (Fine Beam Dual polarisation) mode and SRTM/SIR-C SAR ScanSAR mode (https://directory.eoportal.org/web/eoportal/satellite-missions/s/srtm).

Platform/Instrument Mode	ALOS/PALSAR [23]	SRTM/SIR-C SAR ScanSAR
Centre Frequency	1.27 GHz	5.3 GHz
PRF	1500–2500 Hz	1344–1550 Hz
Range Sampling Frequency	32 MHz (FBS)/16 MHz (FBD)	Transmit pulse width 34 μs
Chirp Bandwidth	28 MHz (FBS)/14 MHz (FBD)	10 MHz
Polarisation	HH + HV or VV + VH	HH and VV
Off-nadir angle	9.9°–50.8°	15°–55°
Swath Width	70 km (FBS, FBD @34.3°)	225 km
Ground Resolution	10 m × 5 m (FBS @34.3°) 20 m × 5 m (FBD @34.3°)	30 m × 30 m
Transmission Peak Power	2 kW	1.2 kW

3.2.3. Analysis of Remaining Phase Components

Radar waves of very low frequency propagate through the ionosphere undergoing Faraday Rotation (FR), i.e., rotation of the polarisation vector. This is mainly caused by the anisotropy of Total Electron Content (TEC) in the ionosphere, the values of which were currently very low in the 11-year solar cycle [40]. In addition, most PALSAR acquisitions occur at a local time of 23:00, when TEC activity is also typically low [41].

The radar wave is delayed when it propagates through the troposphere and ionosphere, resulting in φ_{tro} and φ_{ion} respectively. The sum of these two components is called the atmospheric effects. Phase delay through the troposphere is primarily caused by Precipitable Water Vapour (PWV). In hyper-arid regions, such as the Sahara Desert, the temporal and spatial variation of the PWV within an SAR frame is likely to be less significant than over other areas because of the low humidity in this region. To confirm this, the MODerate-resolution Imaging Spectro-radiometer (MODIS) Precipitable Water product (MYD05 in collection 06) and the ERA-Interim (a global atmospheric reanalysis) data from the European Centre for Medium-Range Weather Forecasts (ECMWF) are collected to compute the phase delay differences between two acquisitions, which is called the Atmospheric Phase Screen (APS). The methods used to generate an APS from the MODIS Precipitable Water product and ECMWF data are discussed in [42,43], respectively. The dates and times when these datasets were acquired are listed in Table 3.

Table 3. Acquisition dates and times of ALOS/PALSAR, MODIS PWV, and ECMWF data. (DOY* denotes day of year.)

No.	Date	DOY*	UTC Time		
			ALOS/PALSAR	MODIS PWV Products	ECMWF Simulations
1	13 August 2007	225	21:00:24	11:35	18:00
2	13 February 2008	044	20:58:56	12:25	
3	30 September 2008	274	20:58:25	11:50	
4	31 December 2008	366	21:00:00	12:20	

The phase component φ_{dis} is caused by surface displacement during the time period between the SAR image pair. Surface displacement might be due to crustal movement, groundwater withdrawal, or sand movements in this study site. However, there is no nearby fault [44] and no earthquake was reported from 13 August 2007 to 31 December 2008 [45] over this study site. In a wider region which covers this study area, the land deformation that is caused by groundwater withdrawal is on the level of a few millimetres per year [46]. This will cause an elevation error on the order of 0.5 m when it is wrongly interpreted as φ_{ele_dif}. Sand movements are composed of a mixture of deposition and erosion. However, if the L-band ALOS/PALSAR were to observe sand movements, it would probably result in the de-correlation between two acquisitions.

3.3. Estimation of Penetration Depth

If the differential phase analysed in Section 3.2.3 is mainly caused by a difference between L- and C-band SAR, then we can invert the L-band and C-band Elevation Difference (LCED, L-band minus C-band) by using Equation (4). The differential phase is converted to height by using the Delft Object-oriented Radar Interferometric Software (DORIS) developed by the Technical University of Delft (TUDelft) [47]. The resulting LCED map would indicate the L-band C-band penetration difference if the LCED has a negative shift in the channel areas compared to that of the non-channel areas. Theoretically, LCED on rock outcrops should be zero and be a negative value in the area where there is a fine-grained sand cover.

To confirm this idea, we classified the study area into three classes, i.e., hilly areas, channel areas, and plain areas, by applying a supervised classification method, the Support Vector Machine (SVM) [48], to an ALOS/PALSAR amplitude image, SRTM C-band DEM, and InSAR coherence. These three datasets are chosen for classification because the channel area is most pronounced in these images. The amplitude decreases when the elevation difference increases according to a study of elevation difference between SRTM DEM and ICESat elevations in a wider region in Kufra [49]. Samples fed to the SVM are chosen manually and separated in training and test parts to evaluate the accuracy of the classification.

Finally, histograms of LCED within each group are analysed. For each of these histograms, the mean value of the histogram will be regarded as the penetration depth, which represents all of the measurements in the surface type. The standard error of mean, $\sigma_{SM} = \sigma_{SD}/\sqrt{N}$, can be used to estimate the accuracy of this mean value. The σ_{SD} is the standard deviation of the histogram and N is the number of samples, which is the pixel numbers within the surface type area in this case. Due to the spatial correlation of the LCED map, a variogram can be used calculate the spatial correlation distance, R [50,51]. Therefore, the independent sample numbers, N, can be calculated by dividing the area A of each surface type into areas with a radius of correlation range, which is $N = A/R^2$.

3.4. Validation of the Penetration Depth

The LCED indicates the differing penetration depths between the L-band PALSAR and C-band SRTM. Since SRTM C-band DEM may also detect elevations lower than the surface, it is necessary to validate the SRTM C-band DEM to surface elevations. In the literature, the SRTM C-band DEM shows an average penetration depth of 1.7 m when compared with SRTM X-band DEM and around 7–9 m when compared with ICESat data over glaciers in the Pamir–Karakoram–Himalaya [52]. The SRTM X-band DEM shows systematic bias from SRTM C-band DEM, which is pronounced in Africa and South America [53]. ICESat elevations are considered to represent the surface elevations over glaciers and peatland areas [52,54]. Therefore, we employ the land altimetry product (GLA14) from ICESat as a reference. ICESat is an earth observation mission primarily designed for measuring ice sheet mass balance from 2003 to 2009. ICESat/GLA14 elevation data is acquired by altimetry LiDAR and has a vertical accuracy up to 0.04 m [26,55,56]. The land altimetry of ICESat is carried out over footprints of a 70 m diameter and spaced every 150 m. The ICESat altimetry data is referenced to TOPEX/Poseidon. We transformed the vertical datum of all datasets to be the same WGS84 ellipsoid.

4. Results

4.1. Comparison of Image Surface Morphology

Figure 6 shows different types of images regarding their surface morphology over the Uweinet Tributary in Kufra. Firstly, the Landsat images (Figure 5a,d) show almost no indication of subsurface channels in this area and no change between 2000 and 2007. Red arrows in the Landsat images (Figure 5a,d) point out three noteworthy areas. They are likely to be sand dunes, which are also recognisable in the SRTM C-band amplitude image (Figure 5b), but cannot be observed in the ALOS/PALSAR image (Figure 5e). The surface may be smooth for L-band (~23.6 cm), but rough for

C-band (~5.6 cm), or the waves from ALOS/PALSAR can transmit through the sand cover in these dunes. The SRTM C-band DEM shows the main channel and its branches, which are incised into the mountains. It is hard to delineate the morphology of short branches or where branches flow into the open areas by examining the SRTM C-band DEM.

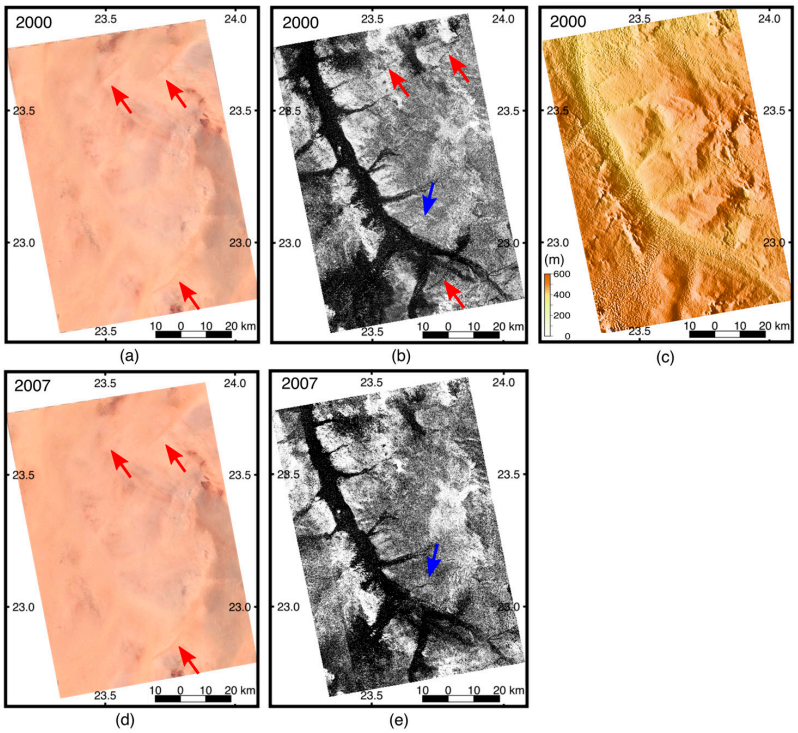

Figure 5. (**a**,**d**) Landsat images in 2000 and 2007 from Google Earth; (**b**) SRTM C-band amplitude image (combined image by sub-swaths 1 & 4 of HH and sub-swaths 2 & 3 of VV); (**c**) SRTM C-band DEM (hill-shaded) showing only the main channels and branches, while hiding small branches. The sand ripples in channel areas can be observed; (**e**) ALOS/PALSAR HH amplitude image. Three red arrows in (**a**,**b**,**d**) point out areas which are likely to be rippled sand dunes, but these areas are unrecognizable in (**c**,**e**). The blue arrow in (**b**,**e**) shows a small branch of the main channel. It is less noticeable in (**b**) than that in (**e**). Years are labeled in the upper left corner of each sub-image.

Both the SRTM C-band amplitude image (Figure 5b) and the ALOS/PALSAR image (Figure 5e) not only clearly display the main channel, but also show some branches. There is a very high contrast between the edges of the channels. As seen from the blue arrow in Figure 5b,e, the ALOS/PALSAR image shows a subtle branch, while in the SRTM amplitude image, no such feature is visible. This observation implies that the ALOS/PALSAR detects deeper subsurface features than the SRTM DEM.

4.2. SAR Interferometry

4.2.1. Interferometic Phase Formation

The temporal and spatial baselines of the four ALOS/PALSAR images were calculated and are shown in Figure 6. Six radar image pairs can, in theory, be formed by using the four radar acquisitions. However, two of the pairs (13 February 2008–30 September 2008 and 13 February 2008–31 December 2008) have large perpendicular baselines beyond 2000 m, which cause difficulties for co-registration. Thus, only four radar image pairs were processed in this study. InSAR processing was applied to the four ALOS/PALSAR InSAR image pairs of 13 August 2007–13 February 2008, 13 August 2007–30 September 2008, 13 August 2007–31 December 2008, and 30 September 2008–31 December 2008.

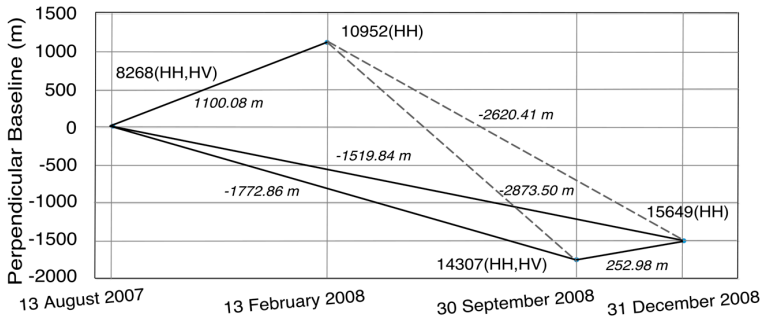

Figure 6. Perpendicular baselines of different InSAR pairs between four ALOS/PALSAR acquisitions (The dates are 13 August 2007, 13 February 2008, 30 September 2008, and 31 December 2008). The number in the figure is the orbit number (8268, 10,952, 14,307, and 15,649). Baselines which are larger than 2000 m are indicated by dashed lines.

4.2.2. Removal of Topographic and Orbital Phase

Topographic phase was simulated by using a C-band SRTM DEM and then subtracting this from the initial interferograms to form differential interferograms. These are shown in Figure 7(a1–a4). These interferograms include all the phase components in Equation (3). The phase ramps in these differential interferograms are along both the range and azimuth directions. These phase ramps may be caused by imprecise baselines which are estimated from inaccurate orbit information of the satellites or can be caused by both orbital inaccuracy and the different atmospheric delay between two acquisitions. In other words, orbital phases and atmospheric phase may be mingled together, and therefore behave as a phase ramp along both the azimuth and range directions [57]. Figure 7(b1–b4) shows the interferograms after baseline refinement. The phase ramps appear to have been successfully removed. Phase distributions in Figure 7(b2,b3) resemble each other, while Figure 7(b1) has more spatial variation and Figure 7(d4) is more uniform in space.

4.2.3. Analysis of Remaining Phase Components

For the analysis of ionospheric effects, we investigated the Faraday rotation angles from the PALSAR catalogue metadata located at the Alaska Satellite Facility (ASF). For SAR acquisitions of 13 February 2008 and 31 December 2008, the estimated Faraday rotation angles are 1.3° and 1.4°, respectively. Besides, the interferograms in Figure 7(b1–b4) do not show noticeable artifacts along the azimuth direction. Therefore, we think that the ionospheric effects have no significant impact on the interferograms and can thus be neglected in this study.

We analysed the tropospheric contributions to the interferograms by using an APS, which can be either calculated from thus ECMWF temperature and pressure data, or from the MODIS Precipitable Water product (MYD05 in collection 06). The results of these two methods are shown in Figure 7(c1–c4),(d1–d4), respectively. It was cloudy on 13 August 2007 in this region, so Figure 7(d1) shows almost no result from the MODIS PWV. We can see from Figure 7(c1–c4) that the APS modelled from the ECMWF temperature and pressure data are uniform in the range direction, but follow a linear trend along the azimuth direction. This may be the azimuth component to the phase ramp in Figure 7(a1–a4), and if it is, it may have been removed with orbital phase during the baseline refinement. The spatial variations of these four APS are much less than 1 radian, which corresponds to an elevation variation of 4.46 m when the perpendicular baseline is 2000 m. However, compared to the APS modelled by ECMWF data, the APS shown in Figure 7(d1–d4) have more spatial variation, which are within 1 radian. According to [58], errors in the derived water vapour of MODIS near-infrared retrieval are estimated to be 5–10%, and errors can be up to 14% under hazy conditions. Considering that new systematic errors may be imported if these APS are not accurate, in this study, we do not subtract the APS from interferograms. We suspect that the interferometric phase in Figure 7(b1) suffers from

the worst atmospheric effects among these four pairs. The spatial similarity between Figure 7(b2,b3) provides indirect evidence that these two pairs do not suffer from serious atmospheric effects.

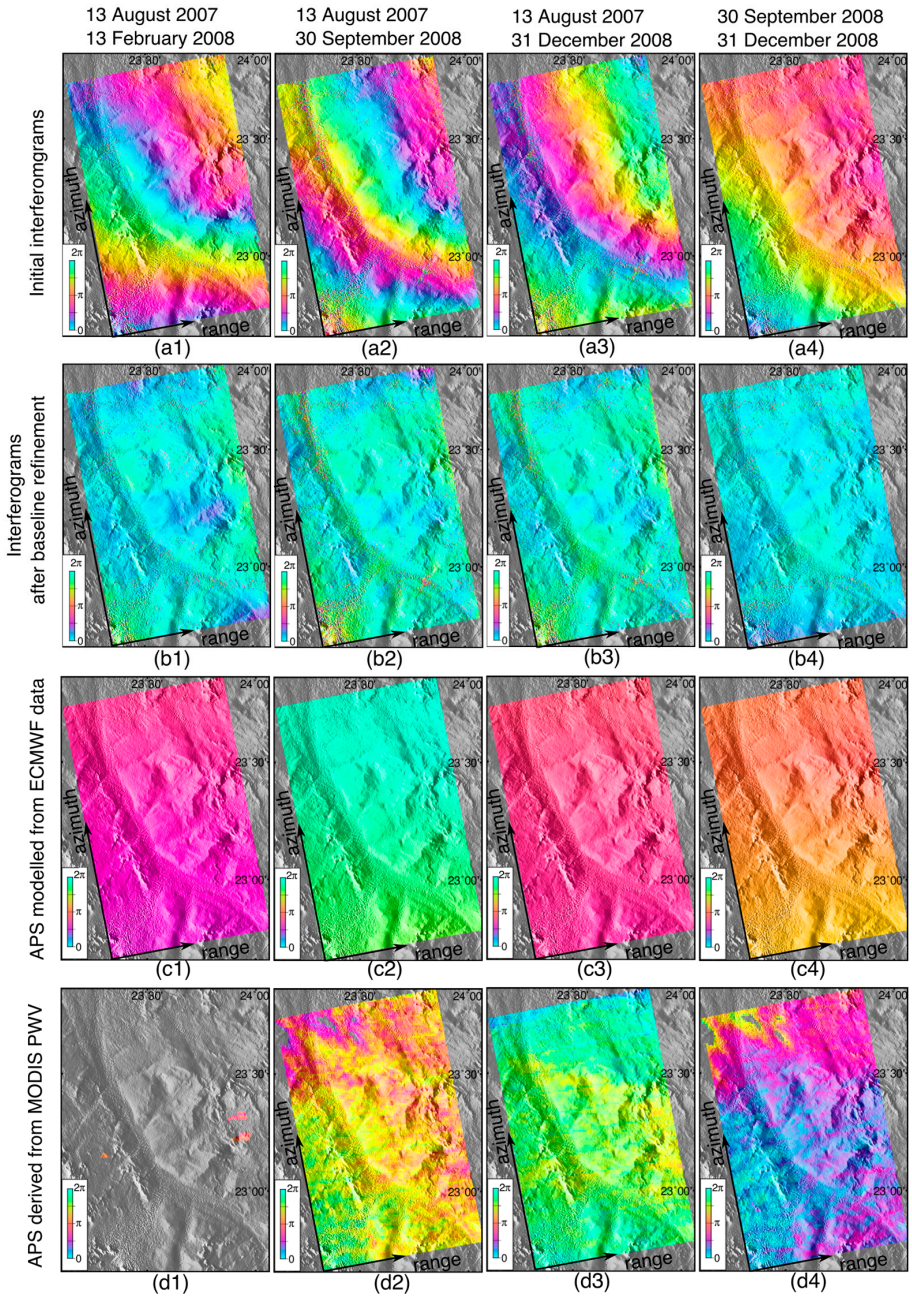

Figure 7. (**a1**–**a4**) Initial interferograms derived from SAR image pairs of 13 August 2007–13 February 2008, 13 August 2007–30 September 2008, 13 August 2007–31 December 2008, and 30 September 2008–31 December 2008; (**b1**–**b4**) Interferograms after baseline refinement. Primary trend of phase variation has been removed; (**c1**–**c4**) Atmospheric Phase Screen (APS) modelled from ECMWF data; (**d1**–**d4**) APS derived from MODIS (Terra L2 product from collection 006) near-infrared Precipitable Water Vapour (PWV). There is almost no data in this area on 13 February 2008 because it was a cloudy day. The absence of data in the upper left corner of (**d2**) and (**d4**) is because cloud appears there on 30 September 2008 (The orbit number is 14307). The striping artifact in (**d1**–**d4**) is caused by well known uncorrected radiometric calibration differences.

4.3. Estimation of Penetration Depth

We converted the remaining phase shown in Figure 7(b1–b4) to the LCED maps which are shown in Figure 8(a1–a4), along with the InSAR coherence maps (Figure 8(b1–b4)). During the conversion, we utilised a reference point (denoted by the white diamond in Figure 8(a1–a4)), which is located at 23.52°N, 23.604°E and is of high coherence, to be the zero-phase reference. We suspect that the first InSAR pair of 13 August 2007–13 February 2008 suffers from severe atmospheric effects because it involves the acquisition on 13 February 2008 when it was cloudy, according to the MODIS observation on this day. Regarding 30 September 2008–31 December 2008, the perpendicular baseline is too short to derive the topographic variation of the interferometric phase. For instance, a topographic variation of 5 m only contributes to a phase change of 0.14 radians within the InSAR frame according to Equation (6). Therefore, we discard two of the InSAR pairs from 13 August 2007–13 February 2008 and 30 September 2008–31 December 2008. The elevation difference caused by the L- and C-band SAR system is a spatial and temporal low-frequency signal in the LCED maps. Two LCED maps in Figure 8(a2,a3) are averaged into a final LCED map to reduce the impact from high-frequency components.

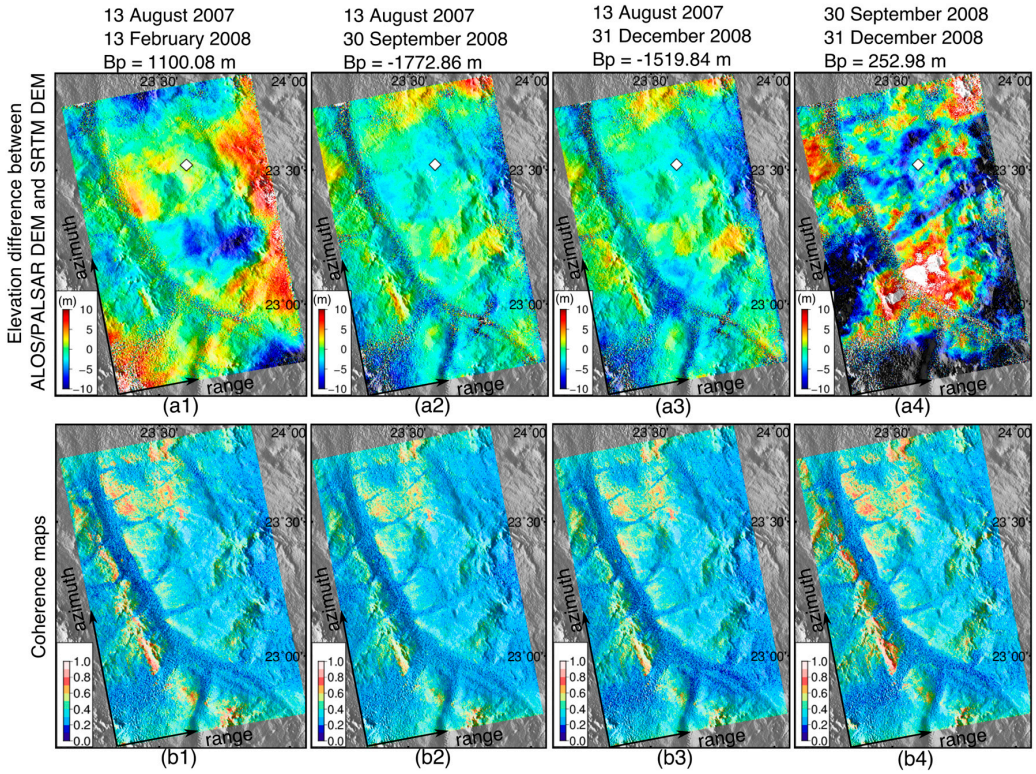

Figure 8. (**a1**–**a4**) Elevation difference maps converted from interferograms shown in Figure 7(b1–b4). These represent elevation differences between ALOS/PALSAR L-band DEMs and SRTM C-band DEMs; (**b1**–**b4**) Coherence maps of the four InSAR pairs.

The ALOS/PALSAR amplitude, SRTM C-band DEM, and the InSAR coherence map are shown in Figure 9a–c. The study site is classified into three groups and the classification result is shown in Figure 9d. Three groups of samples are chosen manually. Samples are divided in a proportion of 50% to 50% for training and testing the SVM classification. The overall accuracy of the classification is 97.2803%.

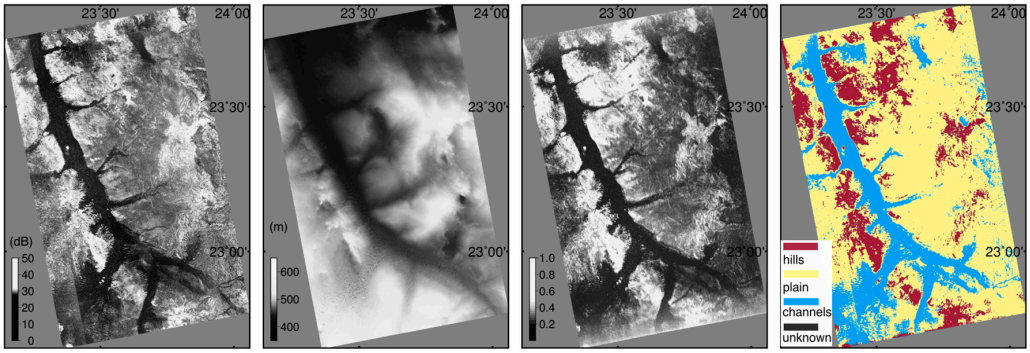

Figure 9. Land surface classification of the study site by using (**a**) the ALOS/PALSAR amplitude image; (**b**) SRTM C-band DEM; (**c**) the averaged coherence map from Figure 8(b1–b4); (**d**) supervised classification result which is generated by applying an SVM (Support Vector Machine) to (**a**–**c**). In this classification, all pixels are classified into four categories, i.e., hills, plains, channels, and unknown.

Figure 10a–c show the histograms of the LCED within each group along with normal distributions fitting to the histograms. From these histograms and normal distributions, we can observe increasing negative elevation differences in the plain and channel areas compared to those in the hilly area. Although some locations in the hilly areas show positive elevation differences, the mean value is still negative, as we can see in Figure 10a. The elevation difference in the hilly area is -0.983 ± 2.284 m, whilst in the plain area and channel area, it is -1.348 ± 2.463 m and -2.744 ± 3.244 m, respectively. The standard deviation is relatively large, which may result from the inclusion of many measurements of low coherence. However, we cannot totally rule these out because the penetration process is more likely to occur where the coherence is low. Thus, we only rule out measurements of coherence lower than 0.218. The larger skewness of the hilly area and channel areas indicate that more measurements tend to show negative shift values of LCED.

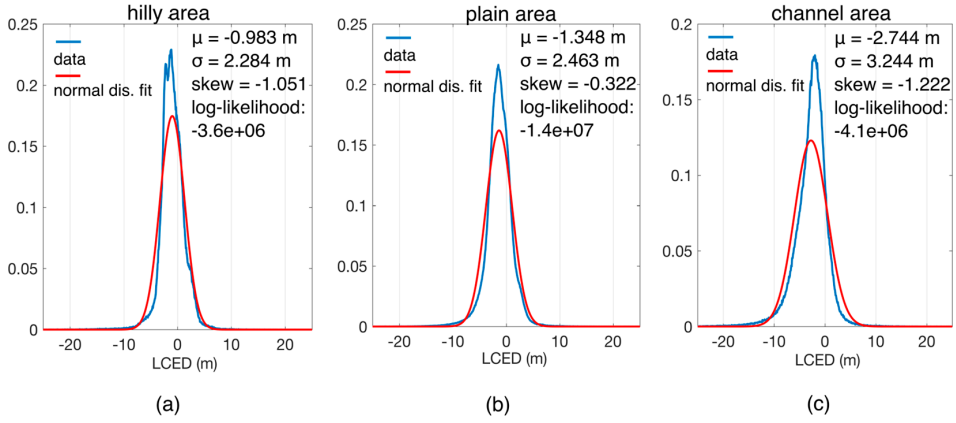

Figure 10. Analyses of elevation difference maps averaged from Figure 8(a2,a3): (**a**–**c**) are the results of fitting the elevation difference with normal distributions in the three types of land surface. Although the coherence is low in the channel and some plain areas, the PALSAR DEM detects lower elevations of 1–3 m than the SRTM DEM.

To evaluate the mean value obtained by the histogram, independent sample numbers need to be considered. We calculated the correlation range of the LCED map, which is about 2.2 km in this study area. The calculation and statistical information is listed in Table 4. According to the calculation in Table 4, the standard errors of the mean are all within 0.1 m, which indicates that the shift we derived is reliable.

Table 4. Statistics of the classification results and effective measurements. (Each pixel denotes an area of ~56 m × 37 m = 2072 m^2).

Statistical Measures	Hilly Area	Plain Area	Channel Area
Numbers of Pixels	1,610,483	6,113,905	1,566,449
Area (A, km^2)	3336.9	12,668.0	3175.2
Range from variogram (R, km)		2.2	
Independent sample numbers ($N = A/R^2$)	1517	5758	1443
Mean (m)	−0.983	−1.348	−2.744
Standard deviation (68.3%) (σ_{SD}, m)	2.284	2.463	3.244
Standard error of mean (68.3%) (σ_{SM}, m) $\sigma_{SM} = \sigma_{SD/\sqrt{N}}$	0.059	0.032	0.085

4.4. Validation of the Penetration Depth by ICESat/GLA14

ICESat has three transects in this study area, which are labelled as ICESat-T1, ICESat-T2, and ICESat-T3 in Figure 11a,b. The base map of Figure 11a is the classification result shown in Figure 9d. The base map of Figure 11b shows the elevation difference, which is averaged from Figure 8(b2,b3). Along these transects, we compared the LCED and elevation difference between SRTM C-band DEM and ICESat elevations. Figure 11(c1–c3) shows the comparisons. From Figure 11(c1–c3), we can see that in the hilly area, both the SRTM DEM and PALSAR DEM agree closely with the ICESat elevations. However, when it comes to the plain and channel areas, both the SRTM DEM and the PALSAR DEM show lower elevations than the ICESat elevations and the PALSAR elevations deviate even more than the SRTM DEM from the ICESat elevation. The red rectangle highlights the area where a shift of elevation difference can be noticed between SRTM DEM and PALSAR DEM. Over the channel area, the PALSAR DEM is noisy due to low coherence; however, it clearly shows that there are lower elevations than either the SRTM DEM or ICESat elevations.

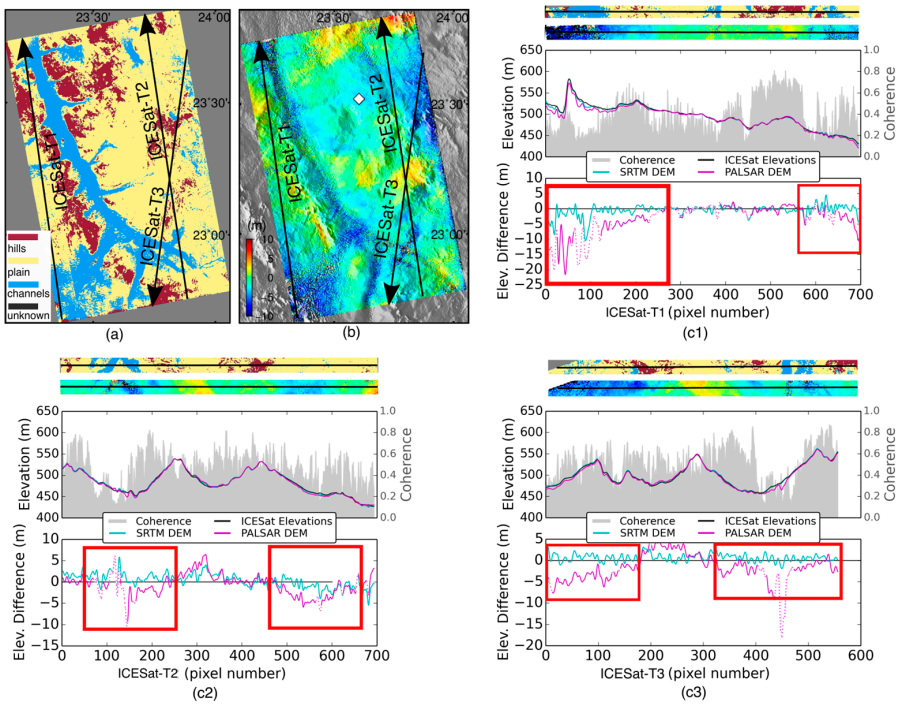

Figure 11. (**a**) The classification result, which is the same as Figure 9d; (**b**) Elevation difference map of the L-band PALSAR DEM and C-band SRTM DEM averaged from Figure 8(a2,a3); (**c1–c3**) Comparisons between ALOS/PALSAR InSAR derived DEM, SRTM DEM, and ICESat elevations along three ICESat transects (ICESat-T1/T2/T3) across the study site. The red rectangles in (**c1–c3**) highlight the areas where there is a negative shift of PALSAR DEM from SRTM DEM and ICESat elevations. The dashed lines in (**c1–c3**) are where the coherence is lower than 0.218.

5. Discussion

This study is aimed at estimating the different penetration depths detected by L-band and C-band SAR. InSAR can measure the terrain variation by using phase differences between two or more acquisitions. When it is applied to L-band and C-band SAR datasets, it can measure different elevations. The accuracy of the elevation difference measured by the InSAR technique depends on internal errors, such as unwrapping errors and baseline errors, and external interruptions, such as atmospheric effects and surface displacement.

The unwrapping error causes a phase ambiguity which leads to a height ambiguity. For the ALOS/PALSAR datasets used in this study, the height ambiguity is 28 m. It indeed exists during InSAR processing on some pixels. However, from the unwrapping results shown in Figure 7(a1–a4) and Figure 7(b1–b4), we can see that most of the pixels in this dataset have been correctly unwrapped. Besides, we analysed the LCED by partitioning the regions and showing all measurements as histograms. There are outliers whose LCED is larger than 28 m in the LCED maps. Their impact on analysing the regional difference of LCED is minimised by using the histograms. The baseline error, which can lead to an error in the height measurement, can be expressed as $\Delta h = \Delta B_{\perp} \cdot h / B_{\perp}$. The height variation in this study site is about 400–600 m, thus, $\Delta B_{\perp}$ of 10 m can cause a height error of 1 m for the ALOS/PALSAR dataset when the perpendicular baseline is 2000 m.

According to Section 4.2.3, the atmospheric phase screen simulated by using ECMWF data features primarily as signals of low spatial frequency. This low-frequency signal can be removed during the baseline refinement. Even though a residual of the atmospheric phase may be preserved in the final unwrapped phase which is converted to the LCED maps, its impact on the LCED is depressed by using long perpendicular baselines, according to the Equation (5). We have discussed the surface displacement in Section 3.2.3. There has not been any earthquake in this region, which could be a source of surface displacement. According to Section 4.1, areas appearing to be rippled sand dunes are observed in SRTM C-band image whilst unobserved in ALOS/PALSAR image. This indicates that sand movements are very likely to be transparent to a L-band SAR system. As for any groundwater withdrawal, it is highly unlikely to cause the elevation shift between the channel and non-channel areas, which is described in Section 4.3.

After considering the internal and external errors of InSAR processing and the observed elevation shifts observed between the channel and non-channel areas, we believe that the remaining phase in Equation (3) is mainly caused by the differences in penetration depths between the L- and C-bands. This difference results from their different penetration depths or different incident angles. When the SRTM DEM has an incidence angle of 60°, the index of refraction needs to be larger than 80 to meet an LCED of 2 m, which is impossible. Otherwise, it may be explained by sand erosion from 2000 to 2008. However, this implies further studies on the locations and changes in the sand deposits and erosions, which is beyond the scope of this study. It may be discussed in the future if sand movement data become available for this study site.

In this study, we regard that the offset of the LCED between the channel and non-channel areas is mainly caused by different penetration depths as it has been reported in several locations in the eastern Sahara [2,4]. Moreover, the increasing negative elevation differences from hilly areas to plain areas, and to channel areas, which are shown in Section 4.3, support this argument. Since the possibility of penetration occurring in the hilly area cannot be excluded, the negative shift of the LCED is about 1.76 m between the hilly and channel areas, which should be the penetration depth if the elevation difference in the hilly area is zero. During InSAR processing, the SRTM DEM was taken as a reference. The comparison between SRTM DEM and ICESat/GLA14 elevations in Section 4.4 demonstrated that the SRTM DEM also detected a subsurface elevation rather than a surface elevation. Therefore, the actual penetration depth of the L-band PALSAR DEM would be the previous estimation of 1–2 m plus SRTM DEM's penetration depth. In conclusion, the ALOS/PALSAR InSAR derived DEM shows an elevation that is at least 1–2 m lower compared with the SRTM and ICESat elevations.

The penetration depth is key to studies related to terrain measurements in regions where there is ice or sand cover. It is especially crucial for the longer wavelength SAR mission, such as L-band ALOS/PALSAR and future P-band BIOMASS. In the future, the methods proposed in this study can be repeated in other deserts, such as the Mojave Desert in South California, USA, Gobi Desert, etc., to estimate the penetration depth. Given more SAR datasets, the phase components from sources like atmosphere and surface displacement can also be analysed in more detail. Currently, limited to a single wavelength (L-band) used by space-borne remote sensing data, a penetration depth of only a few metres can be estimated. It should be noted that the aquifers in the Eastern Sahara have been reported to be of about a 25–100 m depth below ground level in research conducted by the British Geological Survey [59]. Therefore, it is unfeasible to map any aquifer below the Sahara for the present time. However, in the future, low-frequency radar systems including the ESA BIOMASS P-band, as well as even lower frequency radars, may be able to be applied in this field [60], particularly if good corrections can be found for ionospheric distortions at the P-band.

6. Conclusions

This study presents a comparison between ALOS/PALSAR L-band SAR image to Landsat optical image and SRTM C-band amplitude image regarding different surface morphologies that are caused by deeper penetration depth detected by L-band SAR. An L-band and C-band elevation difference map was produced using InSAR and used to estimate the penetration depth in Kufra region. The results show that over one tributary of the paleochannel in Kufra region, the ALOS/PALSAR detects surfaces at least 1–2 m lower than the corresponding C-band SRTM.

The subsurface mapping and the estimation of penetration depth are limited by currently available SAR datasets to L-band frequency, so it is hard to detect some important subsurface features, such as aquifers in hyper-arid regions. However, this study indicates potential for future low frequency SAR missions such as ESA BIOMASS P-band SAR system, which are under development and scheduled to be launched in the early 2020s.

Acknowledgments: We thank the China Scholarship Council (CSC) and University College London (UCL) Dean of MAPS prize who jointly sponsor this work. The authors would also like to thank the ESA-NRSCC DRAGON for their travel support. The authors would finally like to thank the data grant of the 4th ALOS RA (PI No. 1488) led by J.-R. Kim.

Author Contributions: The authors conceived and designed the experiments; S.X. performed the experiments; S.X., J.-P.M. and G.L. analysed the data; S.X. wrote the paper and J.-P.M. edited it.

Conflicts of Interest: The authors declare no conflict of interest.

References

1. Elachi, C.; Granger, J. Spaceborne imaging radars probe 'in depth': New spaceborne radar sensors allow all-weather, day or night, high-resolution imaging of the earth's land and ocean surfaces. *IEEE Spectr.* **1982**, *19*, 24–29. [CrossRef]
2. McCauley, J.F.; Schaber, G.G.; Breed, C.S.; Grolier, M.J.; Haynes, C.V.; Issawi, B.; Elachi, C.; Blom, R. Subsurface valleys and geoarcheology of the eastern Sahara revealed by shuttle radar. *Science* **1982**, *218*, 1004–1020. [CrossRef] [PubMed]
3. Roth, L.; Elachi, C. Coherent electromagnetic losses by scattering from volume inhomogeneities. *IEEE Trans. Antennas Propag.* **1975**, *23*, 674–675. [CrossRef]
4. Schaber, G.G.; McCauley, J.F.; Breed, C.S. The use of multifrequency and polarimetric SIR-C/X-SAR data in geologic studies of Bir Safsaf, Egpyt. *Remote Sens. Environ.* **1997**, *59*, 337–363. [CrossRef]
5. Robinson, C.A.; El-Baz, F.; Al-Saud, T.S.M.; Jeon, S.B. Use of radar data to delineate paleodrainage leading to the Kufra Oasis in the eastern Sahara. *J. Afr. Earth Sci.* **2006**, *44*, 229–240. [CrossRef]
6. El-Baz, F.; Maingue, M.; Robinson, C. Fluvio-aeolian dynamics in the north-eastern Sahara: The relationship between fluvial/aeolian systems and ground-water concentration. *J. Arid Environ.* **2000**, *44*, 173–183. [CrossRef]

7. Robinson, C.; El-Baz, F.; Ozdogan, M.; Ledwith, M.; Blanco, D.; Oakley, S.; Inzana, J. Use of radar data to delineate palaeodrainage flow directions in the Selima Sand Sheet, eastern Sahara. *Photogramm. Eng. Remote Sens.* **2000**, *66*, 745–753.
8. Guo, H.; Liu, H.; Wang, X.; Shao, Y.; Sun, Y. Subsurface old drainage detection and paleoenvironment analysis using spaceborne radar images in Alxa Plateau. *Sci. China Ser. D Earth Sci.* **2000**, *43*, 439–448. [CrossRef]
9. Grandjean, G.; Paillou, P.; Baghdadi, N.; Heggy, E.; August, T.; Lasne, Y. Surface and subsurface structural mapping using low frequency radar: A synthesis of the Mauritanian and Egyptian experiments. *J. Afr. Earth Sci.* **2006**, *44*, 220–228. [CrossRef]
10. Paillou, P.; Schuster, M.; Tooth, S.; Farr, T.; Rosenqvist, A.; Lopez, S.; Malezieux, J.M. Mapping of a major paleodrainage system in eastern Libya using orbital imaging radar: The Kufrah River. *Earth Planet. Sci. Lett.* **2009**, *277*, 327–333. [CrossRef]
11. Paillou, P.; Lopez, S.; Farr, T.; Rosenqvist, A. Mapping subsurface geology in Sahara using L- and SAR: First results from the ALOS/PALSAR imaging radar. *IEEE J. Sel. Top. Appl. Earth Obs. Remote Sens.* **2010**, *3*, 632–636. [CrossRef]
12. Sternberg, T.; Paillou, P. Mapping potential shallow groundwater in the Gobi desert using remote sensing: Lake Ulaan Nuur. *J. Arid Environ.* **2015**, *118*, 21–27. [CrossRef]
13. Grenier, C.; Paillou, P.; Maugis, P. Assessment of Holocene surface hydrological connections for the Ounianga lake catchment zone (Chad). *C. R. Geosci.* **2009**, *341*, 770–782. [CrossRef]
14. Jiao, J.J.; Zhang, X.; Wang, X. Satellite-based estimates of groundwater depletion in the Badain Jaran Desert, China. *Sci. Rep.* **2015**, *5*, 1–5. [CrossRef] [PubMed]
15. Ghoneim, E.; El-Baz, F. The application of radar topographic data to mapping of a mega- paleodrainage in the eastern Sahara. *J. Arid Environ.* **2007**, *69*, 658–675. [CrossRef]
16. Dall, J. InSAR elevation bias caused by penetration into uniform volumes. *IEEE Trans. Geosci. Remote Sens.* **2007**, *45*, 2319–2324. [CrossRef]
17. Wang, R.; Hu, C.; Zeng, T.; Long, T.; Yuan, K. Subsurface Height Measurement Using InSAR Technique in Sand-Covered Arid Areas. In Proceedings of the IEEE International Geoscience Remote Sensing Symposium, Québec, QC, Canada, 13–18 July 2014; pp. 422–424.
18. Elsherbini, A.; Sarabandi, K. Mapping of sand layer thickness in deserts using SAR interferometry. *IEEE Trans. Geosci. Remote Sens.* **2010**, *48*, 3550–3559. [CrossRef]
19. Grandjean, G.; Paillou, P.; Dubois-Fernandez, P.; August-Bernex, T.; Baghdadi, N.N.; Achache, J. Subsurface structures detection by combining L-band polarimetric SAR and GPR data: Example of the Pyla Dune (France). *IEEE Trans. Geosci. Remote Sens.* **2001**, *39*, 1245–1258. [CrossRef]
20. Lasne, Y.; Paillou, P.; August-Bernex, T.; Ruffié, G.; Grandjean, G. A phase signature for detecting wet subsurface structures using polarimetric L-band SAR. *IEEE Trans. Geosci. Remote Sens.* **2004**, *42*, 1683–1694. [CrossRef]
21. NASA. U.S. Releases Enhanced Shuttle Land Elevation Data. Available online: https://www.jpl.nasa.gov/news/news.php?release=2014-321 (accessed on 16 June 2017).
22. Gruber, A.; Wessel, B.; Huber, M.; Roth, A. Operational TanDEM-X DEM calibration and first validation results. *ISPRS J. Photogramm. Remote Sens.* **2012**, *73*, 39–49. [CrossRef]
23. Rosenqvist, A.; Shimada, M.; Ito, N.; Watanabe, M. ALOS PALSAR: A Pathfinder Mission for Global-scale Monitoring of the Environment. *IEEE Trans. Geosci. Remote Sens.* **2007**, *45*, 3307–3316. [CrossRef]
24. Fujisada, H.; Urai, M.; Lwasaki, A. Technical methodology for ASTER Global DEM. *IEEE Trans. Geosci. Remote Sens.* **2012**, *50*, 3725–3736. [CrossRef]
25. Tadono, T.; Ishida, H.; Oda, F.; Naito, S.; Minakawa, K.; Iwamoto, H. Precise global DEM generation by ALOS PRISM. *ISPRS Ann. Photogramm. Remote Sens. Spat. Inf. Sci.* **2014**, *II-4*, 71–76. [CrossRef]
26. Zwally, H.J.; Schutz, B.; Abalati, W.; Abshire, J.; Bentley, C.; Brenner, A.; Bufton, J.; Dezio, J.; Hancock, D.; Harding, D.; et al. ICESat's laser measurements of polar ice, atmosphere, ocean and land. *J. Geodyn.* **2002**, *34*, 405–445. [CrossRef]
27. Tawadros, E. *Geology of Egypt and Libya*; Walter de Gruyter: Berlin, Germany, 2001; p. 608.
28. Conant, L.C.; Goudarzi, G.H. Stratigraphic and tectonic framework of Libya. *AAPG Bull.* **1967**, *51*, 719–730.

29. Paillou, P.; Rosenqvist, A. The SAHARASAR Project: Potential support to water prospecting in arid Africa by SAR. In Proceedings of the IEEE International Geoscience Remote Sensing Symposium, Toulouse, France, 21–25 July 2003; pp. 1493–1495.
30. Hermina, M. The surroundings of Kharga, Dakhla and Farafra Oases. In *The Geology of Egypt*; Taylor & Francis Group, CRC Press: Boca Raton, FL, USA, 1990; pp. 259–292.
31. Lüning, S.; Craig, J.; Fitches, B.; Mayouf, J.; Busrewil, A.; Dieb, M.E.; Gammudi, A.; Loydell, D.; McIlroy, D. Re-evaluation of the petroleum potential of the Kufra Basin (SE Libya, ne Chad): Does the source rock barrier fall? *Mar. Pet. Geol.* **1999**, *16*, 693–718. [CrossRef]
32. Robinson, C.A.; Werwer, A.; El-Baz, F.; El-Shazly, M.; Fritch, T.; Kusky, T. The Nubian aquifer in southwest Egypt. *Hydrogeol. J.* **2007**, *15*, 33–45. [CrossRef]
33. Nubian Sandstone Aquifer System. Available online: https://en.wikipedia.org/wiki/Nubian_Sandstone_Aquifer_System (accessed on 14 April 2017).
34. The Shuttle Radar Topography Mission (SRTM) Collection User Guide. Available online: https://lpdaac.usgs.gov/sites/default/files/public/measures/docs/NASA_SRTM_V3.pdf (accessed on 15 February 2017).
35. Hanssen, R.F. Radar System Theory and Interferometric Processing. In *Radar Interferometry: Data Interpretation and Error Analysis*; Meer, F., Ed.; Kluwer Academic Publishers: Enschede, The Netherlands, 2001; pp. 9–42.
36. ROI_PAC Repeat Orbit Interferometry Package. Available online: http://www.openchannelfoundation.org/projects/ROI_PAC/ (accessed on 15 June 2017).
37. InSAR Principles: Guidelines for SAR Interferometry Processing and Interpretation (ESA TM-19). Available online: http://www.esa.int/About_Us/ESA_Publications/InSAR_Principles_Guidelines_for_SAR_Interferometry_Processing_and_Interpretation_br_ESA_TM-19 (accessed on 15 February 2017).
38. WGS 84 EGM96 15-Minute Geoid Height File and Coefficient File. Available online: http://earth-info.nga.mil/GandG/wgs84/gravitymod/egm96/egm96.html (accessed on 21 May 2017).
39. Chen, C.W.; Zebker, H.A. Phase unwrapping for large SAR interferomgrams: Statistical segmentation and generalised network model. *IEEE Trans. Geosci. Remote Sens.* **2002**, *40*, 1709–1719. [CrossRef]
40. Wegmuller, U.; Werner, C.; Strozzi, T.; Wiesmann, A. Ionospheric Electron Concentration Effects on SAR and InSAR. In Proceedings of the IEEE International Geoscience Remote Sensing Symposium, Denver, CO, USA, 31 July–4 August 2006; pp. 3731–3734.
41. Chen, J.; Zebker, H.A. Ionospheric artifacts in simultaneous L-band InSAR and GPS observations. *IEEE Trans. Geosci. Remote Sens.* **2012**, *50*, 1227–1239. [CrossRef]
42. Li, Z.; Fielding, E.J.; Cross, P.; Preusker, R. Advanced InSAR atmospheric correction: MERIS/MODIS combination and stacked water vapour models. *Int. J. Remote Sens.* **2009**, *30*, 3343–3363. [CrossRef]
43. Jolivet, R.; Grandin, R.; Lasserre, C.; Doin, M.-P.; Peltzer, G. Systematic InSAR tropospheric phase delay corrections from global meteorological reanalysis data. *Geophys. Res. Lett.* **2011**, *38*, L17311. [CrossRef]
44. OneGeology Portal. Available online: http://portal.onegeology.org/OnegeologyGlobal/ (accessed on 21 May 2017).
45. USGS-Earthquake Hazards Program. Available online: https://earthquake.usgs.gov/earthquakes/search/ (accessed on 21 May 2017).
46. Hamling, I.-J.; Aoudia, A. Interaction between the North-West Sahara Aquifer and the seismically active intraplate Hun Graben Fault system, Libya. In Proceedings of the American Geophysical Union (AGU) Fall Meeting, San Francisco, CA, USA, 5–9 December 2011.
47. Kampes, B.; Stefania, U. Doris: The Delft Object-Oriented Radar Interferometric Software. In Proceedings of the 2nd International Symposium on Operationalization of Remote Sensing, Enschede, The Netherlands, 16–20 August 1999; p. 16.
48. Huang, C.; Davis, L.S.; Townshend, J.R.G. An assessment of support vector machines for land cover classification. *Int. J. Remote Sens.* **2002**, *23*, 725–749. [CrossRef]
49. Wang, R.; Muller, J.P.; Hu, C.; Zeng, T. Comparison between SRTM-C DEM and ICESat Elevation Data in the Arid Kufrah Area. In Proceedings of the 2015 IET International Radar Conference, Hangzhou, China, 14–16 October 2015; Institution of Engineering and Technology (IET): Stevenage, UK, 2015; pp. 1–4.
50. Li, G.; Lin, H. Recent Decadal Glacier Mass Balances over the Western Nyainqentanglha Mountains and the Increase in Their Melting Contribution to Nam Co Lake Measured by Differential Bistatic SAR Interferometry. *Glob. Planet. Chang.* **2017**, *149*, 177–190. [CrossRef]

51. Kääb, A.; Treichler, D.; Nuth, C.; Berthier, E. Brief Communication: Contending Estimates of 2003–2008 Glacier Mass Balance over the Pamir–Karakoram–Himalaya. *Cryosphere* **2015**, *9*, 557–564. [CrossRef]
52. Gardelle, J.; Berthier, E.; Arnaud, Y.; Kääb, A. Corrigendum to Region-Wide Glacier Mass Balances over the Pamir-Karakoram-Himalaya during 1999–2011. *Cryosphere* **2013**, *7*, 1885–1886. [CrossRef]
53. Hoffmann, J.; Walter, D. How complementary are SRTM-X and –C band Digital Elevation Models? *Photogramm. Eng. Remote Sens.* **2006**, *72*, 261–268. [CrossRef]
54. Ballhorn, U.; Jubanski, J.; Siegert, F. ICESat/GLAS Data as a Measurement Tool for Peatland Topography and Peat Swamp Forest Biomass in Kalimantan, Indonesia. *Remote Sens.* **2011**, *3*, 1957–1982. [CrossRef]
55. Carabajal, C.C.; Harding, D.J. SRTM C-band and ICESat laser altimetry elevation comparisons as a function of tree cover and relief. *Photogramm. Eng. Remote Sens.* **2006**, *72*, 287–298. [CrossRef]
56. Website of NASA Distributed Active Archive Center (DAAC) at NSIDC—Frequently Asked Questions. Available online: https://nsidc.org/data/icesat/faq.html#9_all (accessed on 24 August 2015).
57. Xiong, S.; Zeng, Q.; Jiao, J.; Gao, S.; Zhang, X. Improvement of PS-InSAR Atmospheric Phase Estimation by Using WRF Model. In Proceedings of the IEEE International Geoscience Remote Sensing Symposium, Québec, QC, Canada, 13–18 July 2014; pp. 2225–2228.
58. Li, Z.; Muller, J.-P.; Cross, P. Comparison of precipitable water vapour derived from radiosonde, GPS and Moderate-Resolution Imaging Spectroradiometer measurements. *J. Geophys. Res. Atmos.* **2003**, *108*. [CrossRef]
59. MacDonald, A.M.; Bonsor, H.C.; Calow, R.C.; Taylor, R.G.; Lapworth, D.J.; Maurice, L.; Tucker, J.; Ó Dochartaigh, B.É. Groundwater Resilience to Climate Change in Africa. In *British Geological Survey Open Report, OR/11/031*; British Geological Survey: Nottingham, UK, 2011; pp. 1–25.
60. Buis, A. NASA Mars Research Helps Find Buried Water on Earth. Available online: http://www.jpl.nasa.gov/news/news.php?release=2011-290 (accessed on 16 June 2017).